Supplementary Information (SI) for Journal of Materials Chemistry A.

Electronic structure tuning to facilitate charge transfers in Z- Scheme mediated CuO/Se@WO_3 aided by synchronized Cu $(OH)_2$ for efficient overall water splitting

Nitul Kalita, Upasana Nath, Anjana Singha, Manabendra Sarma, Mohammad Qureshi
Department of Chemistry
Indian Institute of Technology Guwahati
E-mail: mq@iitg.ac.in (Mohammad Qureshi)

1.1 Dimension of the hetero-structured model and potential energy curves (PECs):

Figure S1 (a) shows a 16.20 Å × 20.70 Å box, where a 4 × 5 CuO, 3 × 4 WO_3, and 6 × 2 $Cu(OH)_2$ supercell structure is considered with lattice mismatch lower than 5%. However, we have considered a smaller heterostructure model for computational viability. In the smaller model, we have taken a 10.61 Å ×10.41 Å cell, where rather than applying any strain to the structure, we have placed one surface over another in such a way that replicates the heterostructure model shown in Figure S1(a) and display in Figure S1(b). In the smaller heterostructure, 2×2 CuO, 2×2 WO_3, and 3×1 $Cu(OH)_2$ supercells have been used.

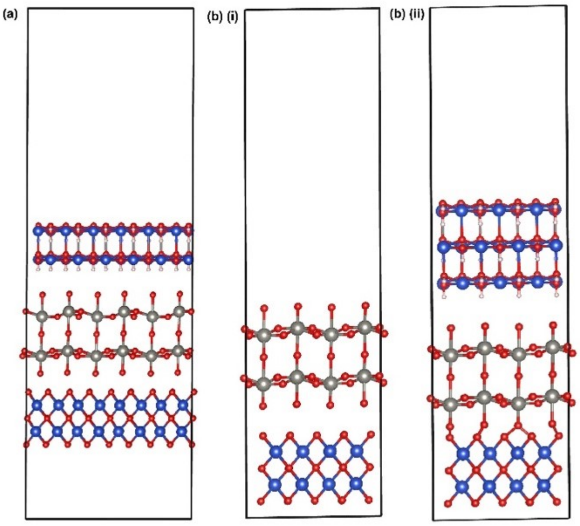

Figure S1: (a) CuO/WO_3/$Cu(OH)_2$ with lattice parameter 16.20 Å × 20.70 Å. (b) CuO/WO_3/$Cu(OH)_2$ with lattice parameter 10.61 Å ×10.41 Å. (i) CuO/WO_3: WO_3 placed over the CuO in such a way that their orbital overlap is similar to Figure R1(a). (ii) CuO/WO_3/$Cu(OH)_2$: Similarly, WO_3/$Cu(OH)_2$ are placed over WO_3.

1.2 Interlayer distances

CuO/WO_3 or CuO/Se@WO_3 heterostructure built by stacking a CuO and WO_3 or Se@WO_3 supercell. The interlayer distance between the layers was determined by the potential energy curve (PECs), as shown in Figure S2. Similarly, the PECs for the interlayer distance between WO_3/$Cu(OH)_2$ and Se@WO_3/$Cu(OH)_2$ are shown in Figure S3 by fixing the interlayer distance between CuO/WO_3 or CuO/Se@WO_3.

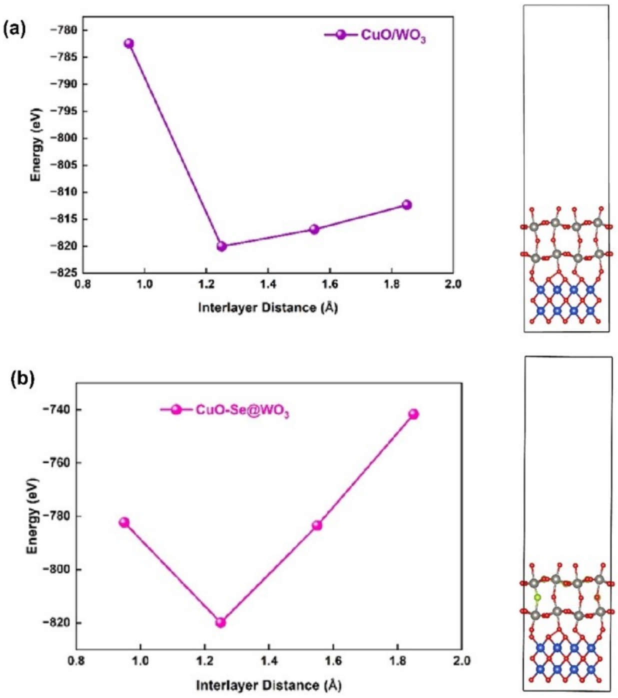

Figure S2: Potential energy curve (PECs) (a) CuO/WO_3 and (b) CuO/Se@WO_3.

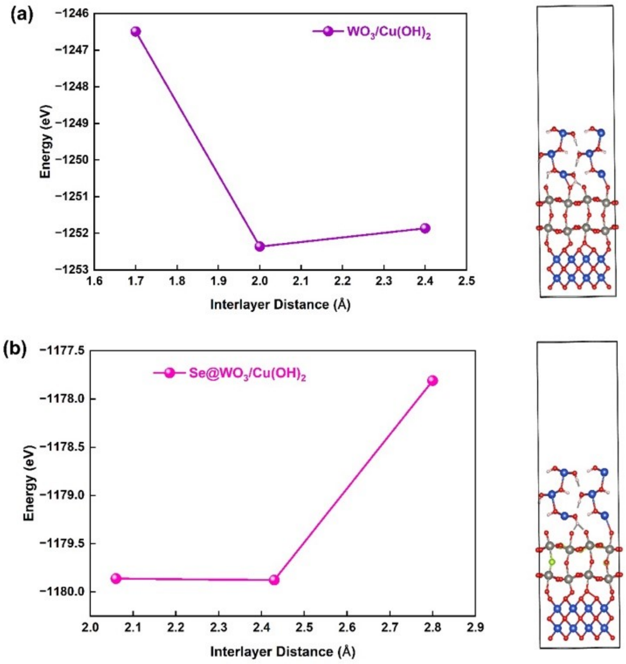

Figure S3: Potential energy curve (PECs) (a) WO_3/ $Cu(OH)_2$ and (b) Se@WO_3/ $Cu(OH)_2$.

1.3 Defect formation energy calculation:

The defect formation energy (E_{df}) can be calculated as[1]**:**

$$E_{df} = E_{Se@WO_3} - E_{WO_3} + n_O\mu_O - n_{Se}\mu_{Se} \tag{1}$$

Here, $E_{Se@WO_3}$ and E_{WO_3} are the energies of the Se@WO_3 and WO_3, respectively. n_O and n_{Se} represent the number of O-atoms removed and the Se-atoms attached, respectively. μ_O and μ_{Se} are the chemical potentials of O and Se, determined by using the isolated O_2 and bulk-Se phase, respectively.[2,3] Hence, the calculated E_{df} of Se@WO_3 was found to be as low as 1.69 eV/atom.

2. Final structure of the composite material used for the theoretical analysis:

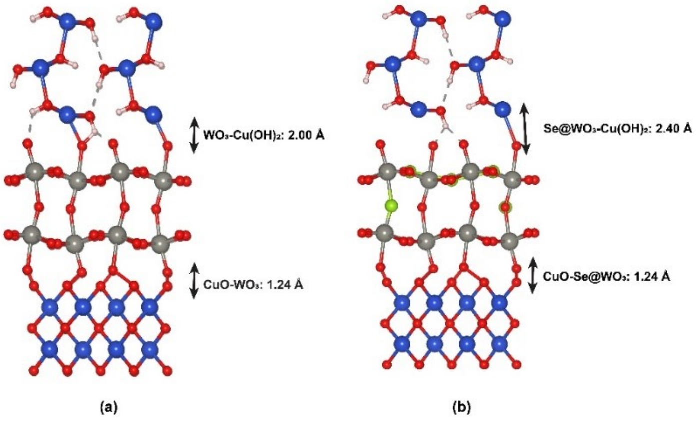

Figure S4: Structure of (a) CuO/WO_3/$Cu(OH)_2$ and (b) CuO/Se@WO_3/$Cu(OH)_2$

3. XRD analysis illustrating the crystallographic changes induced by Se doping in WO_3:

The check the purity of the synthesized WO_3, we have separately synthesized both WO_3 and Se-doped WO_3 on nickel foam substrate, and their comparative XRD analysis has been conducted (Figure S5). From the XRD pattern it has been observed that for WO_3 exhibited peaks at 2θ values 37.2°, 43.3°, and 62.8°, corresponding to the (103), (032), and (150) planes of the monoclinic phase of WO_3 (ICSD No. 00-043-1035). For the Se doped WO_3 (Se@WO_3), peaks were observed at 2θ values 29.7°, 37.2°, 43.3°, and 62.8°, which corresponded to the (211), (103), (032), and (150) planes of WO_3, in agreement with ICSD No. 01-072-0677.

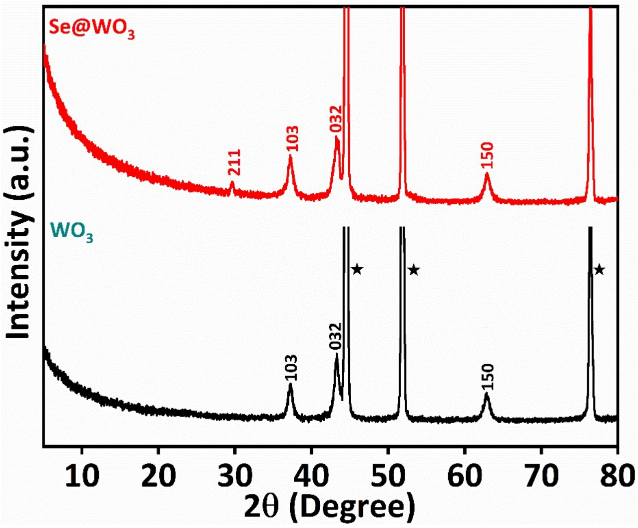

Figure S5: XRD data for WO_3 and Se@WO_3

4. Electrocatalytic activity surface area (ECSA) estimation:

To determine the electrochemical surface area (ECSA), which is indicative of the number of electrochemically active sites in an electrocatalyst, cyclic voltammetry measurements of CuO, CuO/WO3, $CuO/WO_3/Cu(OH)_2$ and CuO/Se@$WO_3/Cu(OH)_2$ electrodes were done (shown in figure S6) in the range of 1.15 and 1.22 V vs. RHE with scan rates of 1-6 mV/s (non-Faradic region). To achieve this, the catalyst was carefully extracted from the Ni foam substrate through a sonication process, followed by centrifugation to isolate the material. 1 mg catalyst powder was then uniformly drop-cast onto the glassy carbon electrode for subsequent electrochemical measurements. Double layer capacitance (C_{dl}), which gives a direct estimate of ECSA value, was calculated from the plot of the difference in current density (j_{anode} - $j_{cathode}$ at 1.21V vs RHE) against the scan rate (Figure 2(g), main manuscript), where C_{dl} is equal to half of the obtained slope value.

ECSA is proportional to the C_{dl} value as follows,

$$\mathrm{ECSA}=\frac{C_{dl}}{C_s} \tag{2}$$

To calculate the ECSA value, we have to determine the C_s (specific capacitance of the material) value by synthesizing an atomically smooth planar surface, which is not practical. But it has been found that for alkaline medium (NaOH), the C_s value for all the materials varies in the range of 0.022–0.130 mF/cm^2, and in general, the average C_s value considered is 0.040 mF/cm^2

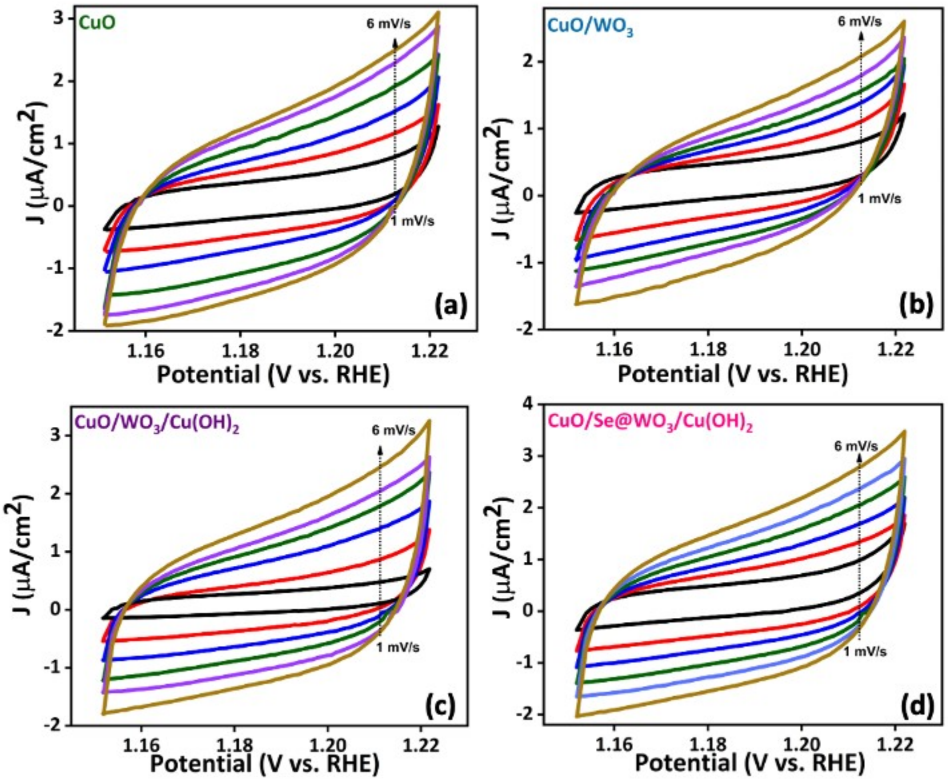

Figure S6: Cyclic voltammetry plots at scan rates ranging from 1 mV/s to 6 mV/s under alkaline conditions in a three-electrode electrochemical cell taken at the non-faradaic region for the catalyst (a) CuO, (b) CuO/WO_3, (c) CuO/WO_3/$Cu(OH)_2$ and (d) CuO/Se@WO_3/$Cu(OH)_2$ composited over glassy carbon electrode

5. Optimization of Se doping on WO_3 for best electrocatalytic activity:

To optimize the doping percentage of selenium (Se) on tungsten trioxide (WO_3) for enhanced electrocatalytic activity, we performed doping using cyclic voltammetry (CV) with varying cycle numbers ranging from 5 to 20. The number of CV cycles was used as a controlled parameter to modulate the amount of Se incorporated into the WO_3 matrix. The resulting selenium-doped WO_3 (Se@WO_3) were used in the composites were then fabricated into electrodes, and their electrocatalytic performance was evaluated through linear sweep voltammetry (LSV). Notably, the electrocatalyst synthesized using 10 CV cycles demonstrated the most favorable performance. All electrodeposition processes were conducted using a 1 mM SeO_2 solution, as described in detail in the materials synthesis section of the main manuscript.

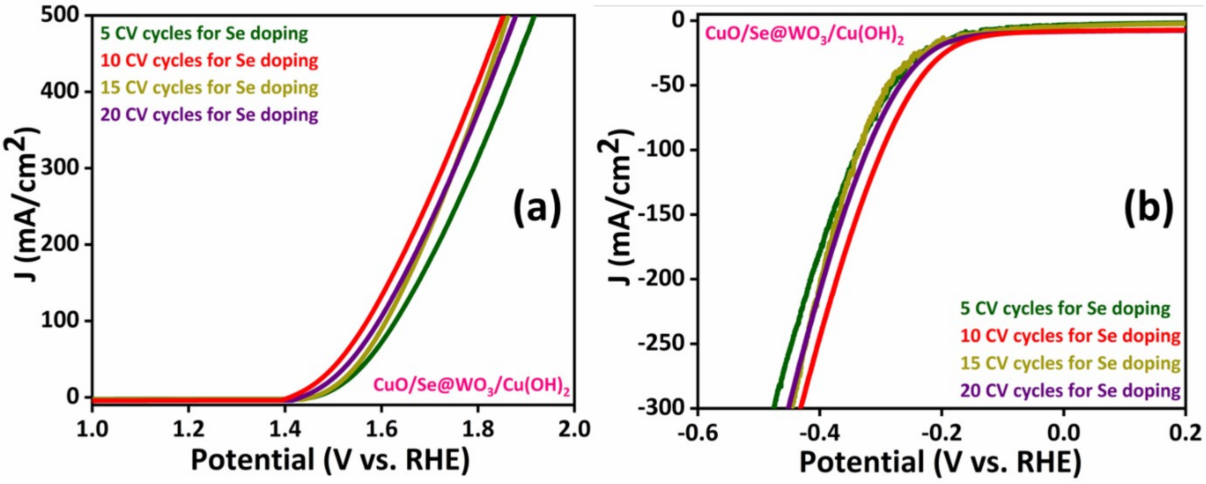

Figure S7: Optimization of Se doping to determine the ideal doping percentage for enhanced performance in (a) OER and (b) HER

6. Scanning transmission electron microscopy energy-dispersive spectrometry (STEM-EDS):

To determine the doping percentage of selenium (Se) substituting oxygen in WO_3, energy-dispersive spectrometry (EDS) was performed on Se@WO_3. The analysis was performed on the optimized Se-doped WO_3 sample, which demonstrated the highest electrocatalytic activity. The analysis revealed that 6% of the oxygen in WO_3 was replaced by selenium atoms.

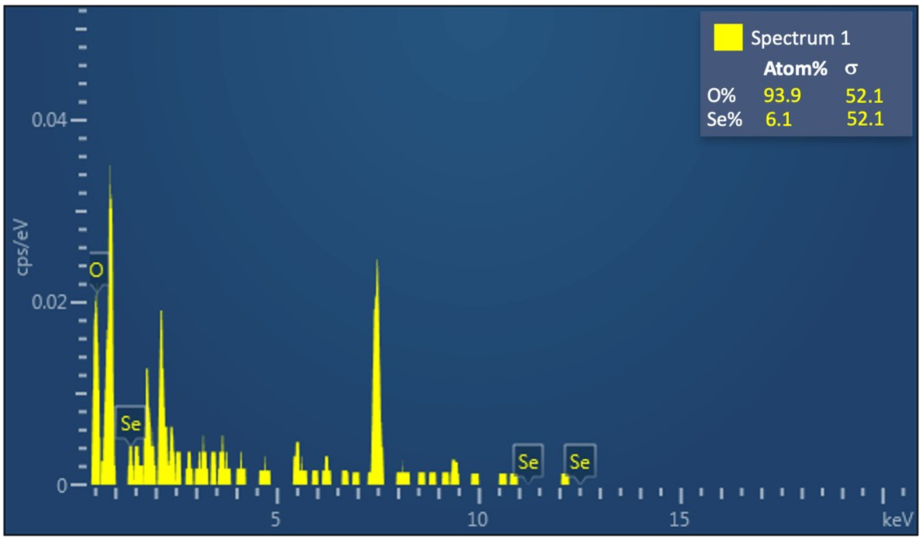

Figure S8. STEM-EDS analysis done on Se@WO_3 to show the doping percentage of Se, replacing oxygen from WO_3

7. Rietveld refinement:

To investigate this cell volume expansion resulting from the Se doping, Rietveld refinement of the XRD data was performed, during the refinement we have excluded the peaks originating from the Ni foam substrate. The cell volume and their respective cell parameters after the refinement has been reported in the Table S1.

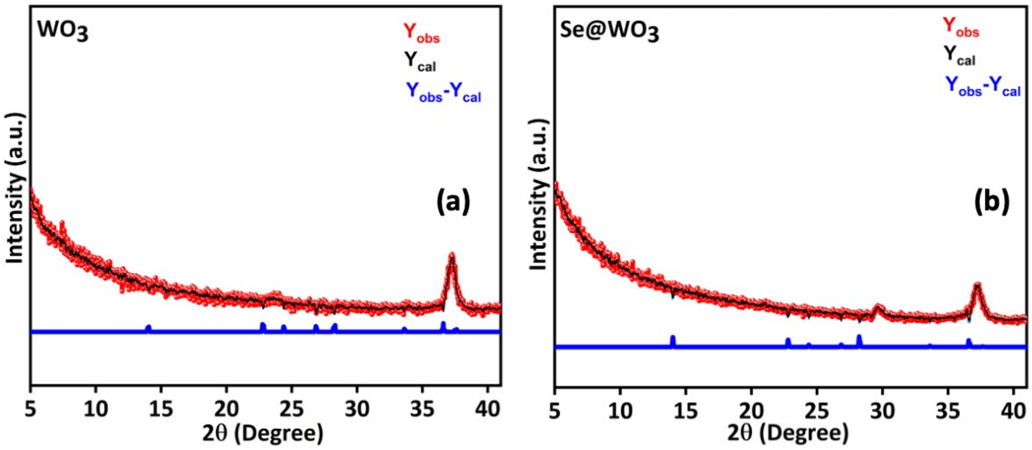

Figure S9. Rietveld refinement of powder XRD of (a) WO_3 and (b) Se@WO_3

Table S1. Rietveld refinement parameters table for WO_3 and Se@WO_3

Materials	a (Å)	b (Å)	c (Å)	α	β	γ	Volume
WO_3	7.3380	7.5810	7.6050	90.000	91.890	90.000	422.790
Se doped WO_3	7.3069	7.5406	7.6930	90.000	90.880	90.000	423.820

8.1 Mott-Schottky analysis:

To determine the semiconductor nature of the materials, Mott-Schottky analysis was conducted. The negative slope of CuO identified it as p-type and the positive slope of WO_3 and Se@WO_3 represent it as n-type semiconductor. This measurement was also utilized to calculate the charge carrier density (N_D).

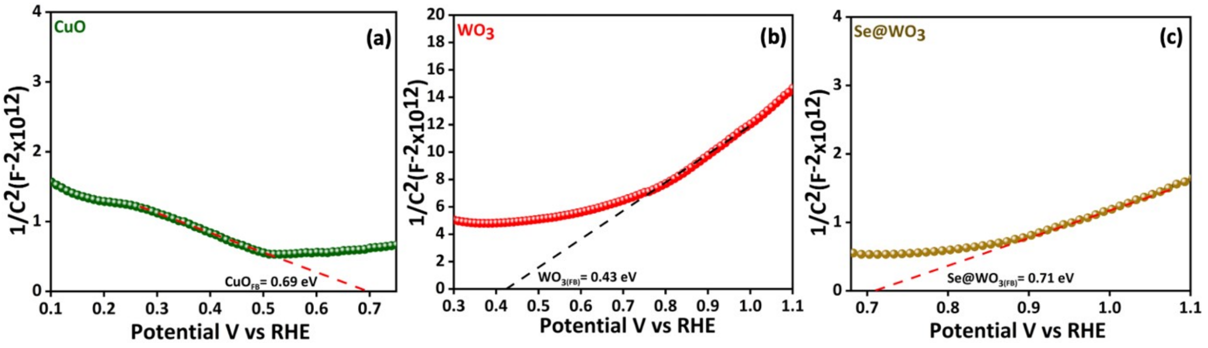

Figure S10. Mott-Schottky plots for (a) CuO, (b) WO_3 and (c) Se@WO_3

To validate the mechanism and charge transfer process, we calculated the carrier density (N_D) for Se@WO_3 before and after the formation of the p-n heterojunction. The results indicate that the carrier density of Se@WO_3 decreased from **6.7×10^{17} cm^{-3} to 5.9×10^{17} cm^{-3}** after the junction formation. This observation confirms the Z-scheme mechanism, as electrons transfer from the conduction band (CB) of Se@WO_3 to the valence band (VB) of CuO. The N_D values were determined using the following relation:

$$\frac{1}{C^2} = \frac{2}{A^2 N_D e \varepsilon \varepsilon_o}\left[E - E_{FB} - \frac{kT}{e}\right] \tag{3}$$

where E_{FB}, A, C and ε are the flat-band potential, exposed surface area, capacitance and the dielectric constant of the photoanode, e is the charge of electron, ε_0 is the permittivity of vacuum, T is the temperature, E is the applied bias and k is the Boltzmann constant.

The Mott Schottky plot that has been used for the deamination of N_D for Se@WO_3 before and after the heterojunction formation has been shown in Figure S11.

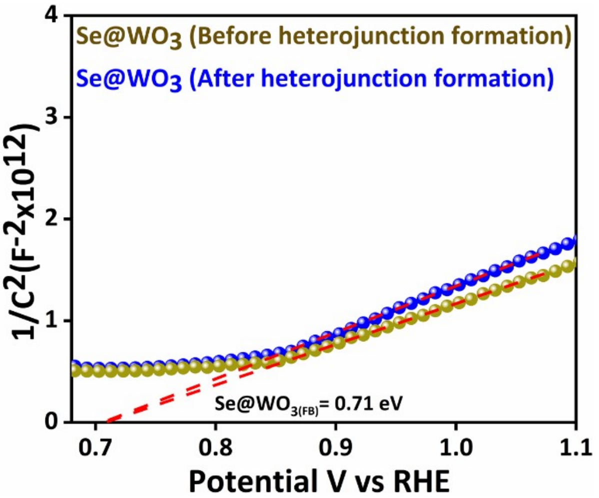

Figure S11: Mott-Schottky plots of Se@WO_3 recorded before and after heterojunction formation

8.2 Calculation involved in career density (N_D) determination:

The career density of a n-type semiconductor can be calculated using the slope of the Mott-Schottky plote with the following formula:

$$N_D = \frac{2}{q * \varepsilon_0 * \varepsilon_r * slope} \qquad (4)$$

Where q is the electronic charge (1.6×10^{-19} C)

ε_0 is the permittivity of free space (8.5×10^{-14} F/cm)

ε_r is the relative dielectric constat (given as 5.03 for WO_3)

Slope is the slope of the Mott-Schottky plot (determined to be 3.95×10^{11} & 4.49×10^{11} for the Se@WO_3 before and after the heterojunction formation)

Substituting values: $N_D =$

$$\frac{2}{(1.6 \times 10^{-19}) * (8.85 \times 10^{-12}) * 5.3 * (3.95 \times 10^{11})}$$

$= 6.74 \times 10^{17}$ cm^{-3} (Se@WO_3 before heterojunction formation)

$N_D =$

$$\frac{2}{\left(1.6 \times 10^{-19}\right) * \left(8.85 \times 10^{-12}\right) * 5.3 * \left(4.49 \times 10^{11}\right)}$$

$= 5.93 \times 10^{17}\ \mathrm{cm}^{-3}$ (Se@WO_3 after heterojunction formation)

9. Tafel analysis of the synthesized electrocatalyst:

Tafel analysis is utilized for relating the rate of an electrochemical reaction to the overpotential. The Tafel slope shows how efficiently an electrode can produce current in response to change in applied potential. The Tafel equation in an electrochemical reaction is given as,

$$\ln I = \ln I_0 + \left(\frac{\alpha n F}{RT}\right)\eta \tag{5}$$

Where **I** is the current, $\mathbf{I_0}$ is the exchange current (current at equilibrium potential), **α** is the charge transfer coefficients for the catalytic reaction, n is the number of electrons transferred, **F** is the Faraday constant (96,485 C), **R** is the ideal gas constant, **T** is the absolute temperature and η is the overpotential.

The equation has the form of y = b + mx and will give a linear line when log I is plotted vs. η, which is the well-known 'Tafel plot'. The slope of the linear line is given as follows,

$$\text{Slope}\left(\frac{d\log I}{d\eta}\right) = \left(\frac{2.303RT}{\alpha n F}\right) \tag{6}$$

Thus, the equation provides a clear view that the slope of the Tafel plot is inversely related to the charge transfer coefficient (α), which means that the lower the Tafel slope, the faster the charge transfer across the electrocatalytic interface.

10. Electrochemical impedance spectroscopy (EIS):

Electrochemical impedance spectroscopy (EIS) was employed to evaluate charge mobility at the electrode–electrolyte interface by determining the charge transfer resistance (R_{ct})

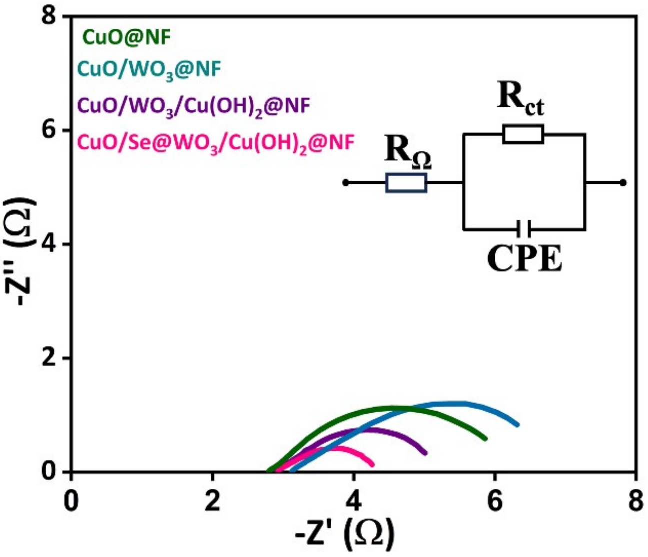

Figure S12. Nyquist plots of all the electrocatalysts measured at a potential of 1.43 V vs the RHE

11. Stability test done through 1000 cycle of continuous cyclic voltammetry:

The durability of the catalyst was evaluated by subjecting the composite material to 1000 cycles of cyclic voltammetry in the Faradaic region. The analysis confirmed the high stability of the electrocatalyst, as negligible changes were observed in the current density values.

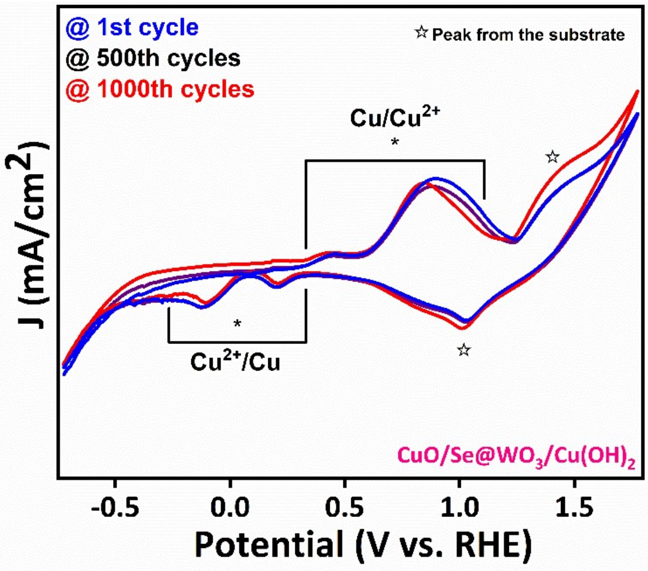

Figure S13. Stability assessment through 1000 cycles of cyclic voltammetry performed in the Faradaic region.

12. X-ray photoelectron spectroscopy (XPS) valence band spectra:

X-ray photoelectron spectroscopy (XPS) valence band spectra provide a reliable approach for determining the positions of valence bands in materials. This technique involves analyzing the valence band spectrum to identify the valence band maximum (VBM), which corresponds to the highest occupied energy state below the Fermi level. The VBM is typically determined by extrapolating the leading edge of the valence band spectrum to the baseline.

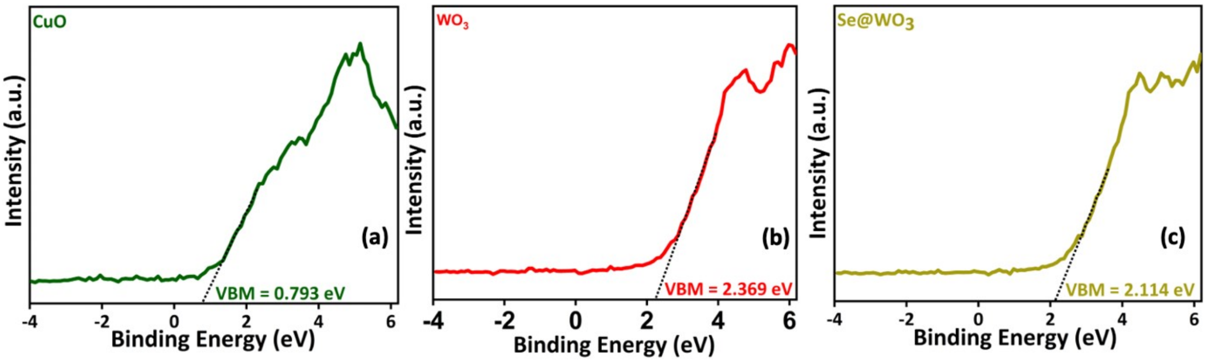

Figure S14. Valence band XPS spectra for (a) CuO, (b) WO_3 and (Se@WO_3)

13. Band gap analysis from Tauc plots:

Tauc plots are a widely used method for determining the band gap energy **(E_g)** of materials. These plots are derived from ultraviolet-visible diffuse reflectance spectroscopy (UV-Vis

DRS) data, typically obtained over a specified wavelength range. By analyzing the absorption spectra, the Tauc plot is constructed by plotting **(αhν)**^{2} against the photon energy (**hν**), where **α** is the absorption coefficient, **h** is Planck's constant, **ν** is the frequency of the light The band gap energy is determined by extrapolating the linear portion of the plot to intersect the photon energy axis (**hν**), where the intercept corresponds to the band gap.

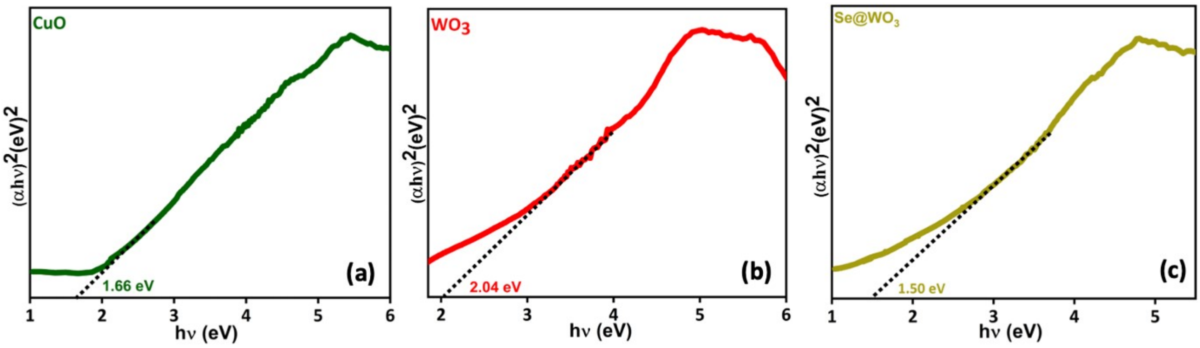

Figure S15: Tauc plot of (a) CuO, (b) WO3 and (c) Se@WO$_3$

By the combining the Tauc plot and XPS valence band spectra, we have determined the band positions of the material, as presented in the table below.

Table S2. Summary of the band positions of the materials determined from the Tauc plot and XPS valence band spectra.

Material	Band Gap (eV)	Valance Band (eV)	Conduction band (eV)
CuO	1.66	0.79	-0.87
WO$_3$	2.04	2.37	0.33
Se@WO$_3$	1.50	2.11	0.61

The table above clearly illustrates that Se doping induces band structure contraction, bringing the conduction band of Se@WO$_3$ closer to the valence band of CuO. This alignment facilitates the Z-scheme charge transfer process, effectively separating the electron-hole pairs generated under an applied potential. Furthermore, the electron transfer from Se@WO$_3$ to CuO, as depicted in Figure 3(f) of the main manuscript, is further validated by carrier density calculations from Mott–Schottky analysis before and after p–n heterojunction formation.

14. DRT methodologies:

The Distribution of Relaxation Time (DRT) is a model-independent technique widely used in electrochemical impedance spectroscopy (EIS) analysis to extract meaningful physical and chemical information about a system. It allows for the deconvolution of impedance spectra into characteristic relaxation times, providing insight into different electrochemical processes.

DRT Methodologies: Open-source MATLAB script-based software (DRT Tools) was used to calculate DRT from the impedance data and the Gaussian method was used for data discretization. The DRT plots was obtained from the EIS data using Gaussian basis function and 0.01 regularization parameter. Each peak is defined by its central position, its total area (which corresponds to its effective resistance) and its width.[4]

The related time constant can be calculated by $t=\frac{1}{2\pi f}$. Here, f represents the frequency, and it is independent of the surface area and represents the intrinsic properties of each process.

Regarding parameter selection, the series resistance across the electrolyte and electrode interface possesses very small time constant, with its peak observed around 10^{-4} to 10^{-3} s.

The charge transfer at the electrode/electrolyte interface is more rapid than that of cathode materials delivering the time constant of 10^{-2} to 10^{-1} s.

The diffusion in electrodes or materials is the most sluggish process because the diffusion is only driven by the concentration gradient. The time constant for diffusion reaches more than 10 s to 100 s.[5]

To calculate the contribution from each peak we have to follow the steps given below:

1. We have to find out the total area by summing up all the area of peak, where peak area represents the impedance of the corresponding process.

2. Next step is to find out the total resistance (uncompensated and charge transfer resistances are denoted as R_u and R_{CT}, respectively) from the fitted EIS Nyquist plot.

15. In-depth discussion comparing the calculated HER/OER performance:

For HER reaction, when the H-atom is adsorbed on the O-atom of $CuO/WO_3/Cu(OH)_2$ surface, the free energy barrier is -0.21 eV. Meanwhile, adsorbed of H-atom on the O-atom of the $CuO/Se@WO_3/Cu(OH)_2$ surface, the potential barrier decreases to -0.17 eV. These results demonstrate the effective hydrogen adsorption-desorption process on $CuO/Se@WO_3/Cu(OH)_2$ compared to $CuO/WO_3/Cu(OH)_2$. The adsorption energy (E_{ads}) of the H-atom is relatively low at other sites of $Cu(OH)_2$, such as Cu and H, compared to the O-site. Therefore, we have identified O as the active site for the reaction. Further, in the OER reaction, we observed a small change in overpotential (η) after the Se-doping with the same potential determining step (PDS), i.e., $*H_2O \rightarrow *OH$.

To gain insight into the enhanced HER-OER activity with the Se-doped system, we have calculated the total DOS of $CuO/WO_3/Cu(OH)_2$ and $CuO/Se@WO_3/Cu(OH)_2$ as shown in Figure S16(a). It has been seen that the DOS of the doped system is around 17 eV higher at the E_f as compared to the undoped structure, which facilitates effective charge transfer during the electrocatalytic cycle.[6-8] Further, the d-band center of the $CuO/Se@WO_3/Cu(OH)_2$ system has a downshift of 0.42 eV, leading to the weakened interactions between the intermediate and the surface.[9,10] A similar downshift of the p-band center is observed on the O-atom (the active site) of $Cu(OH)_2$. Hence, the lowering of the d-band center or the p-band center in $CuO/Se@WO_3/Cu(OH)_2$ [Figure S16(b-c)] provides appropriate binding interaction to hydrogen as well as oxygen intermediates and shows better HER and OER performances. Thus, both experimental and theoretical simulations confirm that Se-doping improves the electronic properties of the material, thereby enhancing its electrocatalytic activity.

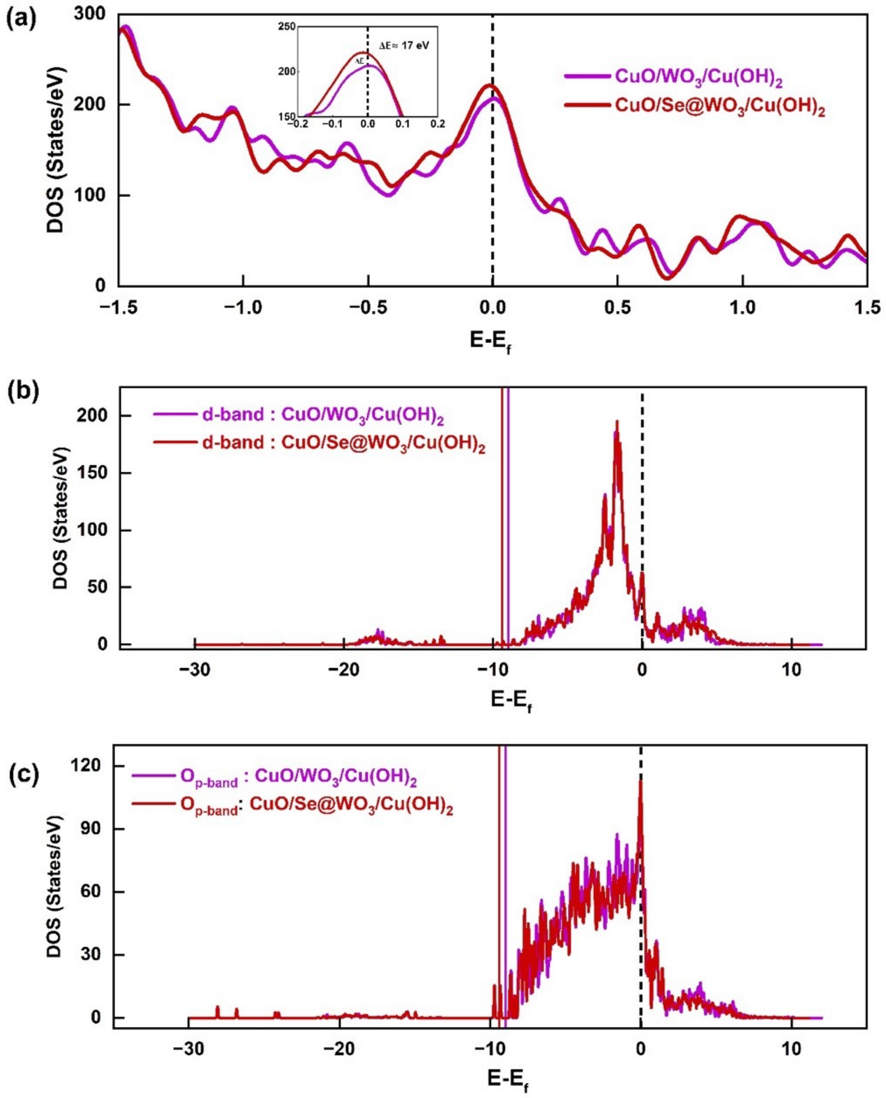

Figure S16: (a) Total density of states (DOS) plot of CuO/WO$_3$/Cu(OH)$_2$ and CuO/Se@WO$_3$/Cu(OH)$_2$. (b) d-orbital DOS of CuO/WO$_3$/Cu(OH)$_2$ and CuO/Se@WO$_3$/Cu(OH)$_2$. (c) p-orbital DOS of O-atom (active center) of Cu(OH)$_2$ of CuO/WO$_3$/Cu(OH)$_2$ and CuO/Se@WO$_3$/Cu(OH)$_2$. Red and purple solid lines represent the band center, and black dotted lines represent the E$_f$.

16. Other supporting computational data:

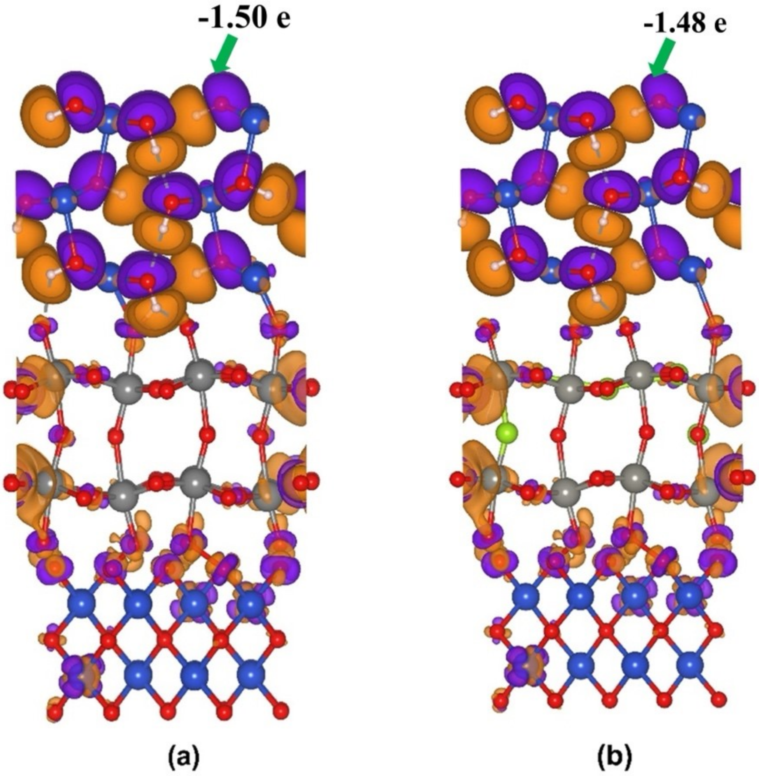

Figure S17: Charge density difference (CDD) plot of (a) CuO/WO$_3$/Cu(OH)$_2$ and (b) CuO/Se@WO$_3$/Cu(OH)$_2$. Purple and orange colors represent the charge accumulation and depletion region, respectively.

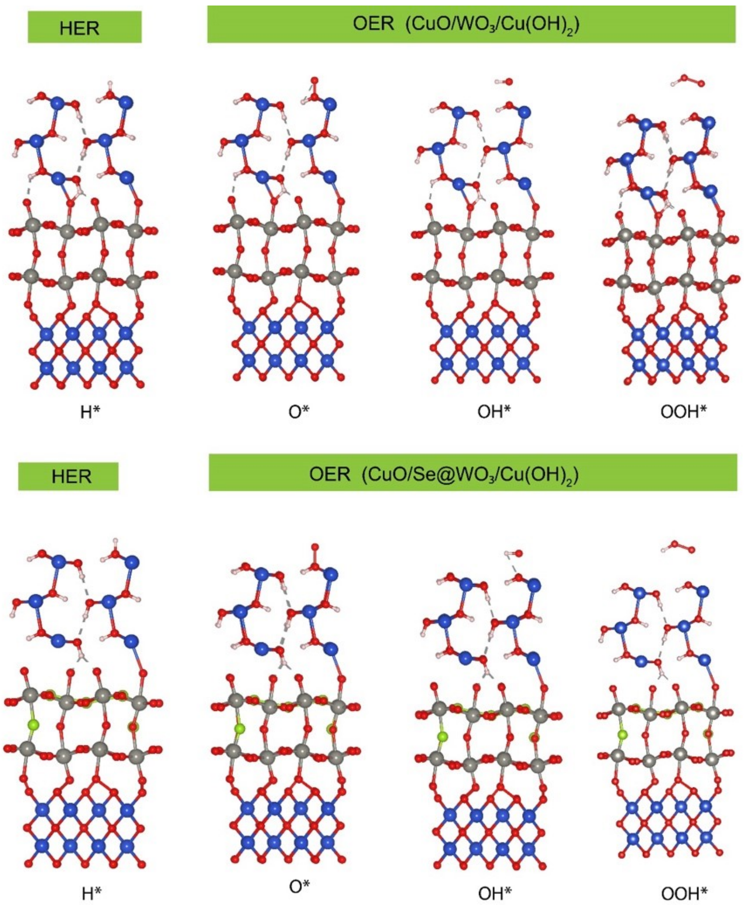

Figure S18: Most preferable adsorption configuration of different intermediates in HER and OER in $CuO/WO_3/Cu(OH)_2$ and $CuO/Se@WO_3/Cu(OH)_2$.

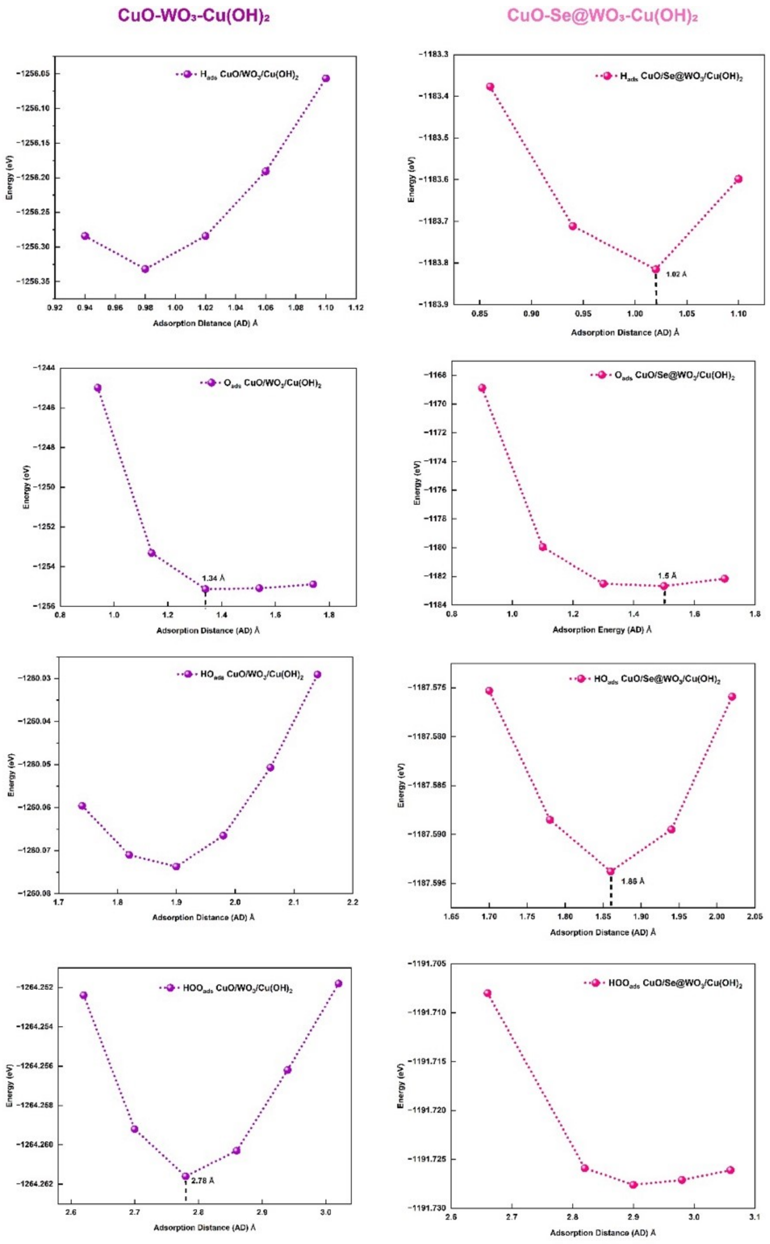

Figure S19: Potential energy plots (PECs) at different adsorption distances to find the stable absorption distance of different intermediate in HER and OER in $CuO/WO_3/Cu(OH)_2$ and $CuO/Se@WO_3/Cu(OH)_2$.

References:

1. Hou, Z., Wang, X., Ikeda, T., Terakura, K., Oshima, M., Kakimoto, M.A. and Miyata, S., 2012. Interplay between nitrogen dopants and native point defects in graphene. *Phys. Rev. B Condens. Matter.* 2012, ***85***, 165439.

2. Khatri, P. and Huda, M.N., Prediction of a new phase of Cu_xS near stoichiometric composition. *Int. J. Photoenergy*, 2015, ***2015***, 478978.
3. Pham, H.H. and Wang, L.W., Oxygen vacancy and hole conduction in amorphous TiO_2. *Phys. Chem. Chem. Phys.*, 2015, ***17***, 541.
4. Y. Lu, C. Z. Zhao, J. Q. Huang, Q. Zhang, The Timescale Identification Decoupling Complicated Kinetic Processes in Lithium Batteries. *Joule* **2022**, 6, 1172
5. S. Shit, W. Jang, S. Bolar, N. C. Murmu, H. Koo and T. Kuila, Effect of ion diffusion in cobalt molybdenum bimetallic sulfide toward electrocatalytic water splitting, *ACS Appl. Mater. Interfaces*, 2019, **11**, 21634
6. Li, Y., Wu, Y., Li, T., Lu, M., Chen, Y., Cui, Y., Gao, J. and Qian, G., Tuning the electronic structure of a metal-organic framework for an efficient oxygen evolution reaction by introducing minor atomically dispersed ruthenium. *Carbon Energy*, 2023 ***5***, e265.
7. Cheng, Y., Fu, P., Yang, X., Zhang, Y., Jin, S., Liu, H., Shen, Y., Guo, X. and Chen, L., $MoP_4/Ni_3S_2/MoO_3$ heterogeneous structure nanorod arrays for efficient solar-enhanced overall water splitting. *J. Mater. Chem. A*, 2023, ***11***, 24764.
8. Wang, T., Wang, P., Zang, W., Li, X., Chen, D., Kou, Z., Mu, S. and Wang, J., Nanoframes of Co_3O_4-Mo_2N heterointerfaces enable high-performance bifunctionality toward both electrocatalytic HER and OER. *Adv. Func. Mater.*, 2022, ***32***, 2107382.
9. Zhang, Y., Zheng, P., Qin, X., Yang, J., Dinh, K.N., Zheng, Y., Shao, M. and Yan, Q., Constructing a multi-bishelled cobalt-based electrocatalyst for the oxygen evolution reaction in CO_2 electrolysis. *NPG Asia Mater.*, 2022, ***14***, 55.
10. Zhang, G., Zhao, L., Li, G. and Xu, L., Thin carbon layer covered Co_4N cubes encapsulated in N-doped porous carbon nanocage as tri-functional catalysts with enhanced charge-transfer efficiency for Zn-air battery and overall water-splitting. *J. Mater. Chem. A*, 2023, ***11***, 11712